Arabian Journal of Chemistry (2022) **15**, 103559

King Saud University

Arabian Journal of Chemistry

www.ksu.edu.sa
www.sciencedirect.com

ORIGINAL ARTICLE

Synthesis, characterization, and anticancer activity of some metal complexes with a new Schiff base ligand

Thamer A. Alorini [a,*], Ahmed N. Al-Hakimi [a,b], S. El-Sayed Saeed [a], Ebtesam Hassan Lutf Alhamzi [c], Abuzar E.A.E. Albadri [a]

[a] *Department of Chemistry, College of Sciences, Qassim University, Buraidah 51452, Saudi Arabia*
[b] *Department of Chemistry, College of Sciences, Ibb University, Ibb, Yemen*
[c] *Department of Biology, College of Science, Sana'a University, Yemen*

Received 24 September 2021; accepted 8 November 2021
Available online 12 November 2021

KEYWORDS

Schiff base complex;
Antibacterial activity;
Antifungal activity;
Anticancer activity;
Nanoparticle

Abstract A new Schiff base ligand, 2-((*E*)-((4-(((*E*)-benzylidene)amino)phenyl)imino)methyl)-naphthalene-1-ol, was prepared by the reflux condensation of *p*-phenylenediamine with 2-hydroxy-1-naphthaldehyde and benzaldehyde. Metal complexes were prepared by reacting the ligand with metal salts: VCl_3, $CrCl_3{\cdot}6H_2O$, $MnCl_2{\cdot}3H_2O$, $FeCl_3{\cdot}6H_2O$, $CoCl_3{\cdot}6H_2O$, $NiCl_2{\cdot}6H_2O$, $CuCl_2{\cdot}2H_2O$, and $ZnCl_2$. The ligand and its metallic complexes were characterized by various techniques such as elemental analysis, AAS, NMR, IR, UV–Vis, TGA, DTA, XRD and TEM. The data confirmed that the ligand coordinated with the metal ions in a bidentate nature, bonding through its azomethine nitrogen atom and phenolic oxygen atom; this gave an octahedral geometry. The XRD patterns of the complexes indicated that they were of various structures: the Mn(II), Co(III), and Cu (II) complexes were triclinic, the ligand and Ni(II) complex were orthorhombic, the V(III) and Zn (II) complexes were hexagonal, the Cu(II) complex was monoclinic, and the Fe(II) complex was cubic. TEM analysis confirmed that the complexes were nanoscale in nature. The antibacterial and antifungal activities of the ligand and its complexes against *Salmonella enterica* serovar typhi and *Candida albicans* were investigated by the hole plate diffusion method. It was observed that the Co(II) and Zn(II) complexes had intermediate antibacterial activities, while the V(III) complex had the highest activity against *C. albicans* fungi. The in vitro anticancer activities of the ligand and its metal complexes were tested towards PC-3, SKOV3, and HeLa tumour cell lines, where they exhibited higher antitumour activities against these selected human cell lines than clinically used drugs such as cisplatin, estramustine, and etoposide.

* Corresponding author.
E-mail address: thamer.ayo@gmail.com (T.A. Alorini).
Peer review under responsibility of King Saud University.

Production and hosting by Elsevier

https://doi.org/10.1016/j.arabjc.2021.103559

1. Introduction

Schiff bases are important chemical compounds in various fields such as inorganic, analytical, and medicinal chemistry due to their versatility; they can form numerous, diverse, stable complexes when they are coordinated with different transition-metal ions. Thus, in recent years, such metal complexes containing Schiff bases have been studied extensively due to their various applications and chemical activities. Schiff bases are formed via the interaction between the carbonyl group of an aldehyde or beta diketone and an amine moiety, and their active group (—N═CH—) contains active electrons, making them ideal candidates for developing new drugs (Al-Hakimi et al., 2020; Maurya et al., 2016). In medicinal chemistry, the development of powerful and effective medicinal drugs has been extensively explored. The derivatives of Schiff bases represent a significant category of compounds that have found multiple applications in therapeutic chemistry because of their wide range of pharmacokinetic properties and their prominence in drug discovery programs (El-Saied et al., 2018). Schiff base derivatives and their complexes have reportedly demonstrated a variety of biological properties, such as anti-inflammatory (Azam et al., 2020; Manimohan et al., 2020), antibacterial (El-saied et al., 2020; Shakdofa et al., 2018), antifungal (Al-Hakimi et al., 2020; Bhaskar et al., 2020), antiviral (Buldurun et al., 2020; Slassi et al., 2020), anticancer (Kavitha and Laxma Reddy, 2016; Mbugua et al., 2020), and antioxidant (Keypour et al., 2020; Radha et al., 2020) activities. Schiff bases also have industrial uses (Betiha et al., 2020; Chauhan et al., 2020) and have been used as highly effective sensors (Hosseinzadeh Sanatkar et al., 2020; Mondal et al., 2020) and catalysts (Bocian et al., 2020; Nagalakshmi et al., 2020), as well as beneficial substances for preserving the environment (Kobisy et al., 2020; Zaman Brohi et al., 2020).

Several published studies have demonstrated the extent to which Schiff bases and their transition-metal complexes exhibit biological activities effective against a range of bacterial and fungal species and tumours. For example, Schiff base complexes have shown antitumor and antioxidative activities, as well as lipid peroxidation inhibition (Yang et al., 2000). This is important as microbial infections have threatened human civilization since ancient times, with large proportions of people dying in various parts of the world due to such diseases. According to a report from the Infectious Diseases Society of America, there are several microbial species that pose serious pathogenic risk; these include *Klebsiella pneumonia* and *Pseudomonas aeruginosa*, as well as species belonging to the *Staphylococcus*, *Enterococcus*, *Enterobacter*, and *Acinetobacter* genuses (Malik et al., 2018). Cancer is another category of deadly diseases, and because they lack proper treatment options they threaten humanity in throughout the developing and developed worlds (Mbugua et al., 2020).

Herein, we report the preparation, characterization, and determination of the crystal structure of a new Schiff base constructed from *p*-phenylenediamine, 2-hydroxy-1-naphthaldehyde, and benzaldehyde as a ligand. Eight complexes derived from this novel base were also prepared. This study assessed the biological activity of the prepared compounds. Namely, all compounds were tested against PC-3, SKOV3, and HeLa tumour cell lines; meanwhile, their antibacterial activities were assayed against *Salmonella enterica* serovar typhi (*S. enterica* ser. typhi) and their antifungal activities were evaluated against Fungus *Candida albicans*.

2. Materials and methods

2.1. Materials and measurements

p-Phenylenediamine, 2-hydroxy-1-naphthaldehyde, and benzaldehyde were purchased from Acros all compounds were of high purity of 98%, while metal salts were obtained from Sigma–Aldrich, ethanol, methanol, dichloromethane, dimethyl sulfoxide (DMSO), and petroleum ether were of analytical grade and purchased from Alfa Aesar and used without purification. ^{1}H and ^{13}C nuclear magnetic resonance (NMR) spectroscopies were performed using a Bruker spectrometer at 850 MHz and 213 MHz, respectively; $CDCl_3$ was used as the solvent, TMS was the standard reference, and the probe temperature was 25 °C. The Fourier-transform infrared (FTIR) spectra of the ligand and its metallic complexes in the solid-state were measured using an Agilent spectrometer (Cary 600 FTIR, USA), which was operated in the wavenumber range of 4000–400 cm^{-1}. UV–Vis spectra of DMSO solutions (1×10^{-4} M) of the ligand and their metal complexes were measured using a Shimadzu spectrophotometer (UV-1650PC, Japan); a 1 cm quartz cell and wavelength range of 250–650 nm were employed. The carbon, hydrogen, and nitrogen contents were determined for the prepared ligand and its metallic complexes using a Eurovector CHN (EA3000, Italy) analyser. The metal elements were determined using AAS (model 200 series AAS spectrometer, Agilent-technologies). TGA and DTA analyses were performed under nitrogen using a Shimadzu simultaneous DTA–TG apparatus (DTG-60AH, Japan); the heating rate was 10 °C/min, the temperature range was 27–525 °C, and Al_2O_3 served as the reference material for the DTA measurements. The XRD patterns of the compounds were collected with a Rigaku XRD diffractometer (Ultima IV, USA). The anode material was Cu Kα (λ = 1.54180 Å) which operated with a current of 30 mA and a voltage of 40 kV. TEM analysis was conducted using a JEOL-100S (Japan) microscope. The molar conductivity (Λ_m) values of the prepared metal complexes dissolved in DMSO (1×10^{-3} M) at room temperature were determined using an Oakton Conductivity/DTS meter. The magnetic sensitivities of the prepared solid metal complexes were measured at room temperature with the Magnetic Susceptibility Balance – Auto from Sherwood Scientific (United Kingdom). *S. enterica* ser. typhi was obtained from the Yemen Standardization, Metrology and Quality Control Organization, while *C. albicans* was obtained from Althubhani Specialist Medical Laboratory (Sana'a, Yemen).

2.2. Preparation of ligand (HL) (1)

The ligand, 2-((*E*)-((4-(((*E*)-benzylidene)amino)phenyl)imino)methyl)-naphthalene-1-ol, was prepared following a literature method (Al-Hakimi et al., 2020), where 1.72 g (0.01 mol) of 2-hydroxy-1-naphthaldehyde and 1.06 g (0.01 mol) of benzaldehyde were dissolved in 20 mL of absolute ethanol and the mixture was stirred until complete dissolution. This solution was then slowly added dropwise to a spherical flask containing 1.08 g (0.01 mol) of *p*-phenylenediamine dissolved in

15 mL of ethanol. The mixture was left to stir under reflux for 3 h, during which an orange precipitate was formed. The precipitate was then filtered and washed several times with distilled water followed by absolute ethanol. Yield: (84%). M.p.: 230 °C. Colour: Orange. IR, $\nu(cm^{-1})$: 3350(m), 1620(s), 1605(s), 1540(s), 1310(m). ^{1}H NMR (850 MHz, $CDCl_3$) (δ, ppm): 6.65–8.10 (m, 15H, Ar–H), 10.05 (s, 1H, N═CH), 10.88 (s, 1H, N═CH), 13.20 (s, 1H, ArOH). ^{13}C NMR (213 MHz, $CDCl_3$) (δ, ppm): 149.9, 149.36, 148.77, 140.35, 133.85, 131.64, 129.63, 128.21, 126.85, 124.85, 123.71, 122.36, 118.07, 117.0, 113.26. UV–Vis (DMSO), λ_{max} (nm): 259, 318. Elemental analysis (%): Calculated: C: 82.27, H: 5.19, N: 7.99; Found: C: 82.03, H: 4.93, N: 7.86.

2.3. Preparation of metal complexes

The ratio of ligand to metal (L:M) was calculated from the molar ratios of several solutions that contained fixed proportions of the metal salt solution with variable quantities of the ligand solution. Mn(II) and Cu(II) metallic complexes (**4** and **8**, respectively) were prepared using $MnCl_2{\cdot}3H_2O$ and $CuCl_2{\cdot}2H_2O$, respectively, in L:M molar ratios of 1:1. V(III), Cr(III), Fe(III), Co(III), Ni(II), and Zn(II) metallic complexes (**2**–**9**, except 4 and 8, respectively) were prepared using VCl_3, $CrCl_3{\cdot}6H_2O$, $FeCl_3{\cdot}6H_2O$, $CoCl_3{\cdot}6H_2O$, $NiCl_2{\cdot}6H_2O$, and $ZnCl_2$, respectively, in L:M molar ratios of 2:1. All the metal complexes were prepared using the following, general method:

An ethanolic solution of the metal salt was mixed with a suitable amount of an ethanolic solution of the ligand in the molar ratios previously mentioned for 3 h on an electric stirrer under reflux at 70 °C. A precipitate was formed, which was then filtered and washed several times with distilled water and then with absolute ethanol to remove the non-reacting organic materials. The solid was then dried in an oven at 50 °C for 2 h.

2.3.1. V(III) Complex (2)

Dark Green precipitate. Yield: (64%). M.p.: 265 °C. IR, $\nu(cm^{-1})$: 3345(m), 1610(s), 1542(s), 1518(s), 1300(m), 620(m), 520(m), 450(s). UV–Vis (DMSO), λ_{max} (nm): 233, 322, 486. Elemental analysis (%): Calculated: C: 70.17, H: 4.29, N: 6.82; Found: C: 70.29, H: 4.12, N: 6.57.

2.3.2. Cr(III) complex (3)

Red precipitate. Yield: (73%). M.p.: 260 °C. IR, $\nu(cm^{-1})$: 3342 (m), 1608(s), 1580(s), 1495(s), 1305(m), 615(s), 535(w), 405(s). UV–Vis (DMSO), λ_{max} (nm): 227, 317, 344, 459, 484. Elemental analysis (%): Calculated: C: 70.08, H: 4.31, N: 6.81; Found: C: 69.94, H: 4.19, N: 6.94.

2.3.3. Mn(II) complex (4)

Burgundy precipitate. Yield: (78%). M.p.: 290 °C. IR, $\nu(cm^{-1})$: 3520–3300(br), 3440(m), 1617(s), 1595(s), 1530(s), 1300(s), 620(w), 570(m), 410(s). UV–Vis (DMSO), λ_{max} (nm): 231, 320, 464, 484, 612. Elemental analysis (%): Calculated: C: 56.27, H: 4.33, N: 5.47; Found: C: 56.70, H: 4.42, N: 5.70.

2.3.4. Fe(III) complex (5)

Dark brown precipitate. Yield: (75%). M.p.: >300 °C. IR, $\nu(cm^{-1})$: 3420–3130(br), 1615(s), 1592(s), 1520(s), 1305(s), 652 (m), 567(m), 425(m). UV–Vis (DMSO), λ_{max} (nm): 261, 318, 379, 463, 487. Elemental analysis (%): Calculated: C: 71.34, H: 4.49, N: 6.93; Found: C: 71.57, H: 4.25, N: 6.67.

2.3.5. Co(III) complex (6)

Brown precipitate. Yield: (81%). M.p.: >300 °C. IR, $\nu(cm^{-1})$: 3330–3030(br), 1615(s), 1594(s), 1515(s), 1305(s), 653(m), 535 (s), 412(m). UV–Vis (DMSO), λ_{max} (nm): 262, 317, 433, 458. Elemental analysis (%): Calculated: C: 71.07, H: 4.47, N: 6.91; Found: C: 70.82, H: 4.38, N: 6.98.

2.3.6. Ni(II) complex (7)

Green precipitate. Yield: (74%). M.p.: >300 °C. IR, $\nu(cm^{-1})$: 3430–3120(br), 3320(m), 1617(s), 1600(s), 1536(s), 1250(m), 619(s), 520(m), 418(m). UV–Vis (DMSO), λ_{max} (nm): 264, 316, 363, 455. Elemental analysis (%): Calculated: C: 71.00, H: 4.59, N: 6.90; Found: C: 70.52, H: 4.51, N: 6.77.

2.3.7. Cu(II) complex (8)

Dark burgundy precipitate. Yield: (75%). M.p.: 270 °C. IR, $\nu(cm^{-1})$: 3520–3230(br), 3443(m), 1612(s), 1544(s), 1511(s), 1298 (s), 634(s), 520(s), 416(m). UV–Vis (DMSO), λ_{max} (nm): 258, 332, 460, 490. Elemental analysis (%): Calculated: C: 55.34, H: 4.26, N: 5.38; Found: C: 55.17, H: 4.06, N: 5.31.

2.3.8. Zn(II) complex (9)

Orange precipitate. Yield: (79%). M.p.: 283 °C. IR, $\nu(cm^{-1})$: 3410(m), 1615(s), 1594(s), 1515(s), 1305(s), 688(m), 534(s), 430(m). UV–Vis (DMSO), λ_{max} (nm): 260, 330. Elemental analysis (%): Calculated: C: 68.87, H: 4.33, N: 6.70; Found: C: 68.64, H: 4.27, N: 6.89.

2.4. Cell culture

The American Type Culture Collection (ATCC) provided the following human cell lines: prostate adenocarcinoma (PC-3), ovarian adenocarcinoma (SKOV3), and cervical cancer (HeLa). Under humid, 5% (v/v) CO_2 conditions, cells were incubated in RPMI-1640 (100 g/mL) enriched with penicillin (100 units/L) and heat-inactivated foetal bovine serum (10% v/v) at 37 °C (Ghfar et al., 2021).

2.5. Cytotoxicity assay

Using the sulforhodamine B (SRB) assay, the cytotoxicities of the prepared chemical compounds were assessed against human tumour cells (PC-3, SKOV3, and HeLa). Before being treated with the chemical compounds, 80% of the confluent proliferating cells were trypsinised and cultivated in a 96-well tissue culture plate for 24 h. Untreated cells (control) were also added to cells that were exposed to the six concentrations of each compound (0.01, 0.1, 1, 10, 100, and 1000 µg/mL). The cells were exposed to the doses for 72 h before being fixed with TCA (10% w/v) for 1 h at 4 °C. After repeated washes, the cells were stained for 10 min in the dark with a 0.4% (w/v) SRB solution. Glacial acetic acid, 1% (v/v), was used to remove any remaining discoloration. The SRB-stained cells were dissolved in Tris-HCl after drying for 12 h, and their colour intensities were quantified using a microplate reader at 540 nm. Using SigmaPlot 12.00 software, the correlation

between the viability percentage of each tumour cell line and the chemical concentrations was analysed to determine the IC_{50} values (i.e., drug dose that reduces survival to 50%) (Alam et al., 2021).

2.6. In vitro antibacterial and antifungal activity

The ligand and its metallic complexes were diluted with DMSO to concentrations of 100 parts per thousand (ppt). All antimicrobial and antifungal activities tests were conducted in the Department of Botany, Laboratory of Microbiology at Sana'a University (Yemen). The antibacterial and antifungal activity assays of the ligand and its metallic complexes were carried out by the hole plate diffusion method (Magwa et al., 2006). Petri dishes were pre-inoculated with the appropriate bacteria and fungi in the following manner:

One hundred μL of the bacteria and fungi suspension was spread over plates containing Mueller–Hinton agar using a sterile cotton swab (Gachkar et al., 2007; Hanbali et al., 2005). Three wide holes (with diameters of 5 mm) were then made in the agar using a cork borer. Different amounts of the compounds (30 μL, 20 μL, and 10 μL) were introduced into each of the holes in appropriately labelled petri dishes using a sterile micropipette. Gentamicin and clotrimazole (10 μg/ mL) were used as positive controls for bacteria and fungi, respectively (El Malti et al., 2007). The bacteria dishes were then incubated at 37 °C for 24 h, while the yeast, mould, and fungi plates were incubated at 28 °C for 24 h, 3 d, and 24 h, respectively. After incubation, the zones of inhibition were measured and recorded. The zone of inhibition was taken to be the diameter of the zone that visibly shows an absence of growth, including the 5 mm well. Additionally, when no inhibition occurred, the value of 0 mm was assigned to the test sample (Magwa et al., 2006).

3. Results and discussion

3.1. Chemistry

Our approach began with the preparation of the ligand (Scheme 1), which was achieved by reacting one equivalent of 2-hydroxy-1-naphthaldehyde with one equivalent of benzaldehyde in absolute ethanol, and then slowly adding the completely dissolved mixture dropwise to one equivalent of *p*-phenylenediamine in 15 mL of ethanol. The metallic complexes were constructed in L:M ratios of 1:1 (Scheme 2) or 2:1 (Scheme 3) by reacting ethanolic solutions of the ligand and various metal chloride salts. All obtained complexes were characterized by FT-IR spectroscopy, UV–Vis electronic absorption, elemental analysis, thermal analysis, X-ray powder diffraction, and TEM, as well as molar conductivity and magnetic susceptibility studies.

3.1.1. ^{1}H NMR spectra

The ^{1}H NMR spectrum of the ligand in $CDCl_3$ (Fig. 1) showed signals consistent with the expected values. Importantly, the spectrum lacked the signal of the amino group (—NH_2) characteristic of the starting material. The spectrum showed one peak as a singlet at 13.20 ppm, which was assigned to the hydroxyl (—OH) moiety (Ren et al., 2020), along with two peaks at 10.88 ppm and 10.05 ppm, which were assigned to the —N═CH— groups; the difference in the shifts of these two protons is due to the polarity of the 2-hydroxy-1-naphthaldehyde moiety, which is in closer proximity to the group whose proton appears at 10.88 ppm (Al-Hakimi et al., 2020). Another signal appeared as a multiplet within the range of 6.65–8.10 ppm, which is attributed to aromatic protons (Al-Hakimi, 2020; Al-Hakimi et al., 2020).

3.1.2. ^{13}C NMR spectra

The ^{13}C NMR spectrum of the ligand (Fig. 2) showed peaks appearing at 149.9, 149.36 and 148.77 ppm. These peaks can be attributed to the C—OH, HC═N, and HC═N groups, respectively. The peaks within the 113.26–140.35 ppm range were assigned to the aromatic carbons (Al-Hakimi, 2020; Al-Hakimi et al., 2020).

3.1.3. Elemental analysis and physical properties

Elemental analysis and physical data (Table 1) supported the proposed structures of the ligand and its metal complexes, with the V(III), Cr(III), Fe(III), Co(III), Ni(II), and Zn(II) complexes showing L:M molar ratios of 2:1 and the Mn(II) and Cu(II) complexes showing L:M molar ratios of 1:1. Furthermore, the molar conductivity values of the complexes indicate that the chloride anions are located within their inner-spheres.

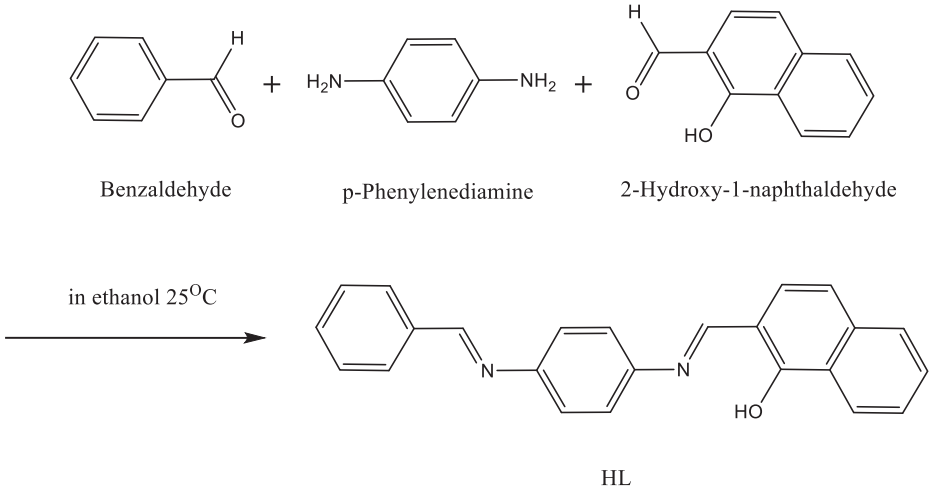

Scheme 1 Preparation of the Ligand.

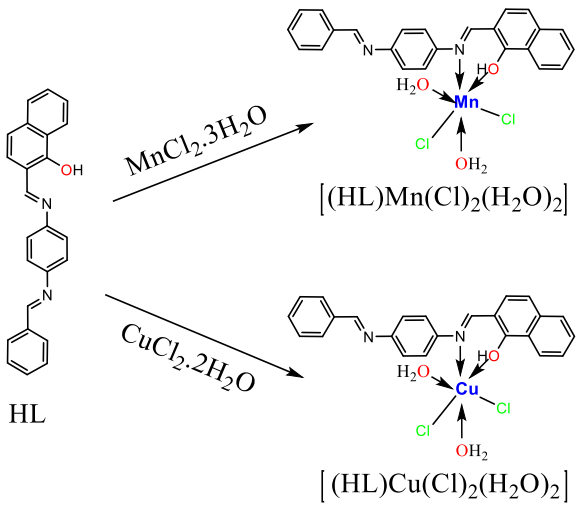

Scheme 2 Preparation of the metallic complexes in ligand-to-metal(L. M) ratios of 1:1.

3.1.4. Molar conductivity

To verify the ionic formulas of the prepared metal complexes in solution, the molar conductivities of DMSO solutions of the complexes (1×10^{-3} M) were determined (Table 1). A range of 6.0–27.3 Ω^{-1} mol^{-1} cm^{-2} was obtained; such low values indicate that the complexes are non-electrolytic in nature (Alhakimi et al., 2021; El-tabl et al., 2008). This confirms that the anions are coordinated with the metal ions in all complexes. To further ensure this absence of an electrolytic nature, a $AgNO_3$ solution was added to the metal complex solutions; as expected, there was no formation of a white precipitate or any turbidity, which confirmed that the chlorine ions are not located outside the coordination sphere as accompanying ions. This supports the proposed shapes of the complexes.

3.1.5. Magnetic susceptibility

The room-temperature magnetic moments of the complexes (**2**–**9**) are shown in Table 1. The V(III) and Ni(II) complexes (**2** and **7**, respectively) show magnetic moments of 2.85 μB, indicating they possess two unpaired electrons in their outer valence shells as well as octahedral geometries (Güngör and Gürkan, 2019). However, the Cr(III) complex (**3**) showed a magnetic moment of 3.9 μB, confirming the presence of three unpaired electrons in its outer valence shell, resulting in an octahedral geometry around the Cr(III) ion (El-Tabl, 2002; El-tabl et al., 2008). The magnetic moment values for the Mn(II), Fe(III), and Co(III) complexes (**4**, **5**, and **6**, respectively) are 5.96, 5.94 and 4.8 μB, respectively, indicating high-spin Mn(II), Fe(III), and Co(III) ions, as well as five, five, and four unpaired electrons in their respective outer valence shells; they also showed octahedral geometries (Murukan and Mohanan, 2006). Cu(II) complex **8** had a magnetic moment of 1.70 μB, which corresponds to one unpaired elec-

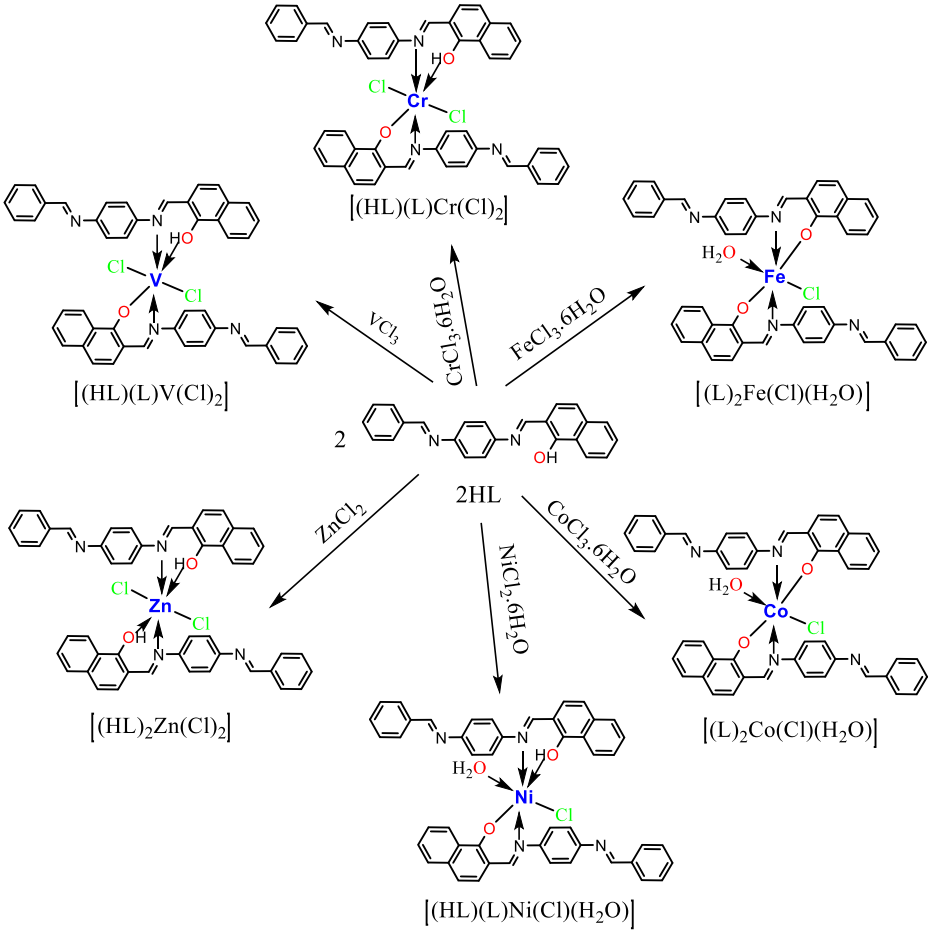

Scheme 3 Preparation of the metallic complexes in L. M ratios of 2:1.

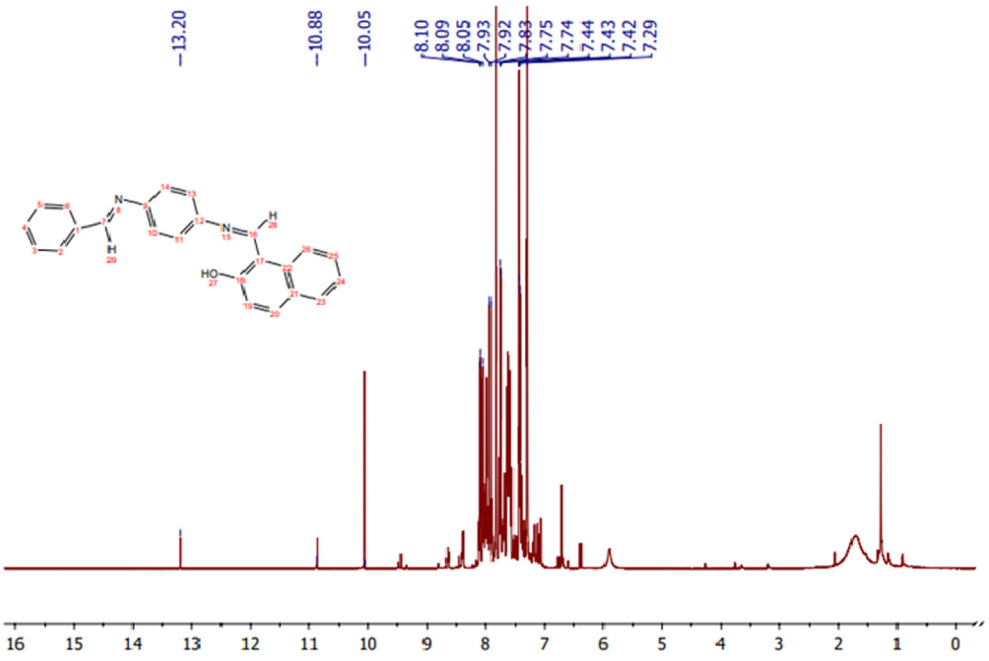

Fig. 1 ^{1}H NMR spectrum of the ligand.

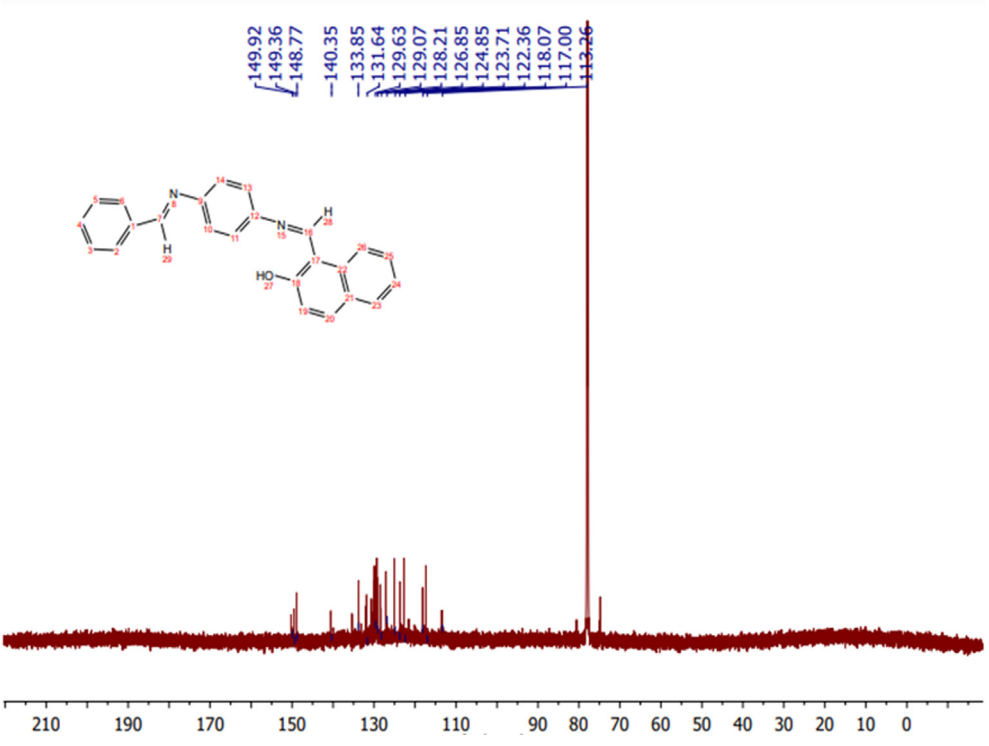

Fig. 2 ^{13}C NMR spectrum of the ligand.

tron and an octahedral geometry (Singh et al., 2017). Finally, the Zn(II) complex (**9**) showed a diamagnetic value.

3.1.6. FT-IR spectra

The important absorption bands of the ligand and its metal complexes are presented in Table 2. The IR spectrum of the ligand (Fig. 3) shows a sharp, weak band centred at 3350 cm^{-1}, which is attributed to the hydroxyl group (ν(O—H)) (AL-FAKEH et al., 2020). The spectrum also shows strong bands at 1620 and 1605 cm^{-1}, which are assigned to the two azomethine groups (ν(C═N)) (Aly et al., 2012; El-tabl et al., 2008). In addition, medium and strong bands

Table 1 Elemental analysis and physical properties of the ligand and its metal complexes.

Comp. No.	Compound (m.w)	Colour	Yield (%)	M.p. (°C)	Ω^{-1} mol^{-1} cm^2	μ_{eff} (μB)	Found (Calc.) (%)			
							C	H	N	M
1	[HL][$C_{24}H_{18}N_2O$] (350.41)	Orange	84	230	–	–	82.03 (82.27)	4.93 (5.19)	7.86 (7.99)	–
2	[(HL)(L)V(Cl)$_2$] (821.66)	Dark Green	64	265	3.8	2.85	70.29 (70.17)	4.12 (4.29)	6.57 (6.82)	6.05 (6.20)
3	[(HL)(L)Cr(Cl)$_2$] (822.72)	Red	73	260	7.4	3.9	69.94 (70.08)	4.19 (4.31)	6.94 (6.81)	6.47 (6.32)
4	[(HL)Mn(Cl)$_2$(H_2O)$_2$] (512.29)	Burgundy	78	290	21.1	5.96	56.70 (56.27)	4.42 (4.33)	5.70 (5.47)	10.78 (10.72)
5	[(L)$_2$Fe(Cl)(H_2O)] (808.12)	Dark Brown	75	> 300	26.9	5.94	71.57 (71.34)	4.25 (4.49)	6.67 (6.93)	6.72 (6.91)
6	[(L)$_2$Co(Cl)(H_2O)] (811.21)	Brown	81	> 300	25.6	4.8	70.82 (71.07)	4.38 (4.47)	6.98 (6.91)	7.14 (7.26)
7	[(HL)(L)Ni(Cl)(H_2O)] (811.98)	Green	74	> 300	8.4	2.85	70.52 (71.00)	4.51 (4.59)	6.77 (6.90)	7.03 (7.23)
8	[(HL)Cu(Cl)$_2$(H_2O)$_2$] (520.89)	Dark Burgundy	75	270	27.3	1.7	55.17 (55.34)	4.06 (4.26)	5.31 (5.38)	12.06 (12.20)
9	[(HL)$_2$Zn(Cl)$_2$] (837.12)	Orange	79	283	6.0	Dia.	68.64 (68.87)	4.27 (4.33)	6.89 (6.70)	7.51 (7.81)

Table 2 FTIR spectral data of the ligand and its metal complexes.

Comp.No.	ν(OH)	ν(H_2O)	ν(C═N)	ν(C═C)	ν(C-O)	ν(M—O)	ν(M—N)	ν(M—Cl)
1	3350	–	1620,1605	1540	1310	–	–	–
2	3345	–	1610,1542	1518	1300	620	520	450
3	3342	–	1608,1580	1495	1305	615	535	405
4	3440	3520–3300(br)	1617,1595	1530	1300	620	570	410
5	–	3420–3130(br)	1615,1592	1520	1305	652	567	425
6	–	3300–3030(br)	1615,1594	1515	1305	653	535	412
7	3320	3430–3120(br)	1617,1600	1536	1250	619	520	418
8	3443	3520–3230(br)	1612,1544	1511	1298	634	520	416
9	3410	–	1615,1594	1515	1305	688	534	430

appeared at 1540 and 1310 cm^{-1}, corresponding to ν(C═C) and ν(C—O), respectively (El-tabl et al., 2008). By comparing the IR spectrum of the ligand with the spectra of the metal complexes, the method of metal–ligand coordination can be elucidated. The ν(O—H) vibrations of complexes **2**, **3**, **4**, **7**, **8**, and **9** were observed as strong bands at 3345, 3342, 3440, 3320, 3443, and 3410 cm^{-1}, respectively (El-tabl et al., 2008). Except for complexes **2**, **3**, and **9**, these complexes also show broad band in the 3520–3030 cm^{-1} range, which is assigned to coordinated water molecules (El-Tabl et al., 2008; Mosa'd Jamil et al., 2018). Medium and strong bands are noted at complexes **2**–**9** in the 1620–1608 cm^{-1} and 1595–1542 cm^{-1} ranges and are due to the ν(C═N) vibrations involving the benzene group and the C═N unit coordinating with a metal ion, respectively (Al-Hakimi et al., 2020; El-tabl et al., 2008). However, in compounds, **1**–**9** the medium and strong bands that appear in the 1536–1495 cm^{-1} and 1305–1250 cm^{-1} ranges are due to ν(C═C) and ν(C—O) vibrations, respectively (El-tabl et al., 2008; El-Tabl et al., 2008). Additionally, complexes **2**–**9** shows medium bands in the ranges of 688–615, 570–520, and 450–405 cm^{-1}, which are due to ν(M—N), ν(M—O), and ν(M—Cl) vibrations, respectively (El-tabl et al., 2008). These results combined with the elemental analysis indicate that the Schiff base coordinated to the metal ions via the hydroxyl oxygen of its naphthaldehyde moiety and the N atom of one of its azomethine groups.

3.1.7. UV–Visible spectra

The electronic spectral data of the ligand (HL) and its metal complexes in DMSO are presented in Table 3. The ligand UV–Vis spectrum (Fig. 4) showed absorbance bands at 318 nm and 259 nm, which may correspond to the n → π^* and $\pi \rightarrow \pi^*$ transitions, respectively, within the aromatic rings in the ligand. On the other hand, these transitions in the complexes appeared as bands that were shifted compared to those of the ligand; specifically, the bands corresponding to the n → π^* and $\pi \rightarrow \pi^*$ transitions appeared in the ranges of 310–332 nm and 227–264 nm, respectively (Al-Hakimi et al., 2020). This indicates bonding between the ligand and the metallic elements. Furthermore, the V(III) complex showed a band at 486 nm representing a $^3T_{1g}$ (F) → $^3T_{2g}$ (P) transition, further indicating an octahedral geometry for the V(III) ion (Dorn et al., 2020). The Cr (III) complex shows three bands at 484, 459, and 344 nm corresponding to the transitions $^4A_{2g}$ (F) → $^4T_{1g}$ (P), $^4A_{2g}$ (F) → $^4T_{2g}$ (F), and $^4A_{2g}$ (F) → $^4T_{1g}$ (F), respectively; this supports the previously identified octahedral geometry of the Cr(III) ion (Tarafder et al., 2000). The Mn(II) complex showed three bands at 612, 484,

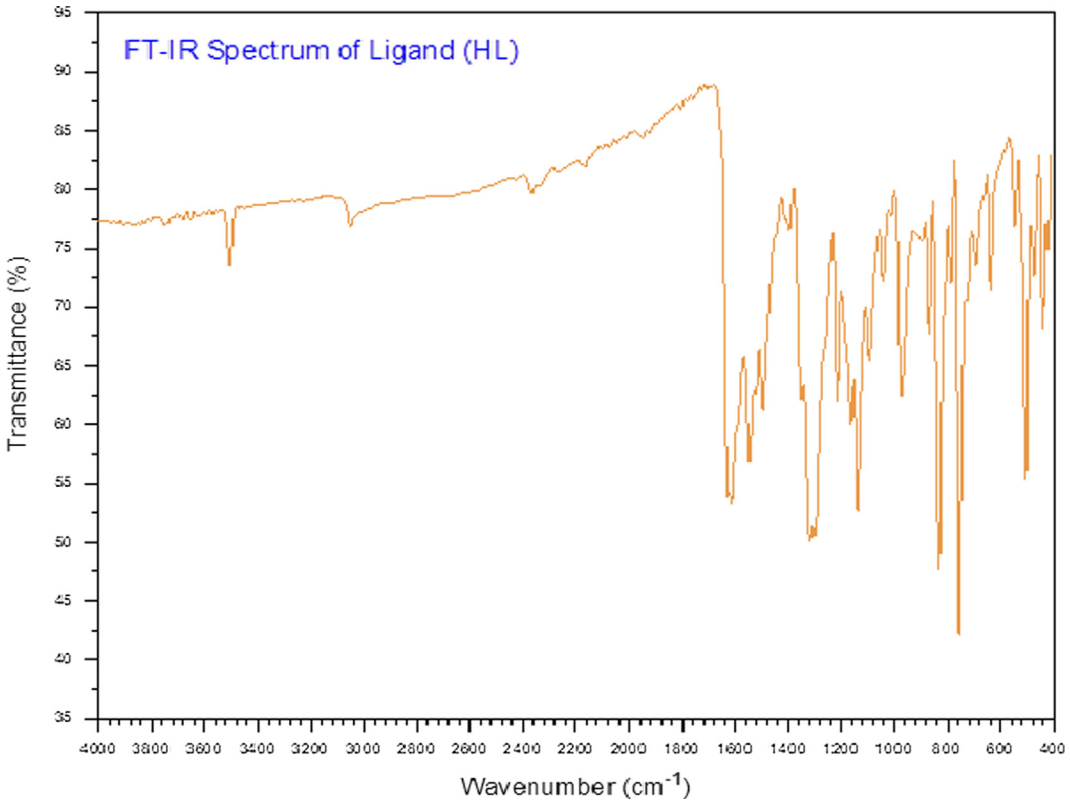

Fig. 3 FT-IR spectrum of the ligand.

and 464 nm that were assigned to $^4T_{1g} \rightarrow {}^6A_{1g}$, $^4T_{2g}$ (G) $\rightarrow {}^6A_{1g}$, and $^4T_{1g}$ (D) $\rightarrow {}^6A_{1g}$ transitions, respectively, suggesting an octahedral geometry around the Mn(II) ion (Mahmoud et al., 2020). The Fe(III) complex showed bands at 487, 463, and 379 nm corresponding to $^4T_{1g}$ (D) $\rightarrow {}^6A_{1g}$, $^4T_{2g}$ (G) $\rightarrow {}^6A_{1g}$, and $^4T_{2g}$ (G) $\rightarrow {}^6A_{1g}$ transitions, respectively, which are indicative of an octahedral geometry (Mahmoud et al., 2020). The Co(III) complex showed two bands at 458 and 433 nm that were assigned to $^4T_{1g}$ (F) $\rightarrow {}^4T_{2g}$ (F) and $^4T_{1g}$ (F) $\rightarrow {}^4A_{2g}$ transitions, suggesting an octahedral geometry for the complex (Mahmoud et al., 2020). The Ni(II) complex showed bands at 455 and 363 nm, which are attributable to $^3A_{2g}$ (F) $\rightarrow {}^3T_g$ (F) and $^3A_{2g}$ (F) $\rightarrow {}^3T_{1g}$ (P) transitions, respectively, indicating an octahedral Ni(II) complex (El-tabl et al., 2008). The Cu(II) complex exhibited bands centred at 490 and 460 nm that were assigned to ligand → metal charge transfer, $^2B_1 \rightarrow {}^2B_2$, and $^2B_1 \rightarrow {}^2E$ transitions, respectively, indicating a distorted octahedral structure (El-tabl et al., 2008). Finally, the Zn(II) complex showed bands at 330 and 260 nm, indicating the presence of intra-ligand transitions and LMCT (Al-Hakimi et al., 2020; El-Tabl et al., 2008).

3.1.8. Thermal analyses (DTA and TGA)

TGA and DTA curves in the range of 27–525 °C were collected for the complexes, which confirmed that they were thermally stable up to 100 °C. The thermal data for the complexes are summarized in Table 4 (El-Saied et al., 2018a; Shakdofa et al., 2021).

3.1.9. XRD analysis

The XRD patterns were recorded for the ligand and its complexes. The crystal structure details for all compounds are listed in Table 5. It was noted that the V(III) and Zn (II) complexes have hexagonal crystal systems. Meanwhile, the ligand and Ni(II) complex have orthorhombic crystal systems, while that of the Cr(III) complex is monoclinic, that of the Fe(III) complex is cubic, and those of the Mn (II), Co(III), and Cu(II) complexes are triclinic. Peak broadening in the XRD patterns signifies that the particles are on a nanometre scale (El-Shafiy et al., 2017). This is supported by the parameters of the crystal structures ranging from 12 nm to 217 nm (Saeed et al., 2014). The XRD patterns of the Co(III), Cu(II), and Zn(II) complexes are shown in Figs. 5, 6, and 7, respectively.

3.1.10. TEM morphological study

TEM was used to further examine the particle sizes and crystallinities of the samples. TEM bright-field images of the ligand and its metal complexes (Figs. 8 and 9) show that the samples comprise small and varying nanoparticles sizes. It can be clearly seen that the metal complex powders show both spherical and rod-shaped nanoparticles, while the ligand powder particles take on rod shapes and are micro-sized. Furthermore, the particles were estimated size of the ligand and metal complexes with a grain size of about 5.0–206.0 nm. These results agree with the XRD data in Table 5.

Table 3 UV–Vis spectral data of the ligand and its metal complexes.

Comp. No.	compounds	λ_{max} (nm)	λ_{max} (cm^{-1})	Assignment
1	$[HL][C_{24}H_{18}N_2O]$	318	31,445	$n \rightarrow \pi^*$
		259	38,610	$\pi \rightarrow \pi^*$
2	$[(HL)(L)V(Cl)_2]$	486	20,576	$^3T_{1g}$ (F) $\rightarrow$ $^3T_{2g}$ (P)
		322	31,055	$n \rightarrow \pi^*$
		233	42,918	$\pi \rightarrow \pi^*$
3	$[(HL)(L)Cr(Cl)_2]$	484	20,661	$^4A_{2g}$ (F) $\rightarrow$ $^4T_{1g}$ (P)
		459	21,786	$^4A_{2g}$ (F) $\rightarrow$ $^4T_{2g}$ (F)
		344	29,070	$^4A_{2g}$ (F) $\rightarrow$ $^4T_{1g}$ (F)
		317	31,546	$n \rightarrow \pi^*$
		227	44,052	$\pi \rightarrow \pi^*$
4	$[(HL)Mn(Cl)_2(H_2O)_2]$	612	16,339	$^4T_{1g} \rightarrow {}^6A_{1g}$
		484	20,661	$^4T_{2g}$ (G) $\rightarrow$ $^6A_{1g}$
		464	12,551	$^4T_{1g}$ (D) $\rightarrow$ $^6A_{1g}$
		320	31,250	$n \rightarrow \pi^*$
		231	43,290	$\pi \rightarrow \pi^*$
5	$[(L)_2Fe(Cl)(H_2O)]$	487	20,533	$^4T_{1g}$ (D) $\rightarrow$ $^6A_{1g}$
		463	21,598	$^4T_{2g}$ (G) $\rightarrow$ $^6A_{1g}$
		379	26,385	$^4T_{2g}$ (G) $\rightarrow$ $^6A_{1g}$
		318	31,447	$n \rightarrow \pi^*$
		261	38,314	$\pi \rightarrow \pi^*$
6	$[(L)_2Co(Cl)(H_2O)]$	458	21,834	$^4T_{1g}$ (F) $\rightarrow$ $^4T_{2g}$ (F)
		433	23,094	$^4T_{1g}$ (F) $\rightarrow$ $^4A_{2g}$
		317	31,546	$n \rightarrow \pi^*$
		262	38,168	$\pi \rightarrow \pi^*$
7	$[(HL)(L)Ni(Cl)(H_2O)]$	455	21,978	$^3A_{2g}$ (F) $\rightarrow$ ^3T_g (F)
		363	27,548	$^3A_{2g}$ (F) $\rightarrow$ $^3T_{1g}$ (P)
		316	31,646	$n \rightarrow \pi^*$
		264	37,879	$\pi \rightarrow \pi^*$
8	$[(HL)Cu(Cl)_2(H_2O)_2]$	490	20,408	$^2B_1 \rightarrow {}^2B_2$
		460	21,739	$^2B_1 \rightarrow {}^2E$
		332	30,120	$n \rightarrow \pi^*$
		258	38,760	$\pi \rightarrow \pi^*$
9	$[(HL)_2Zn(Cl)_2]$	330	30,303	$n \rightarrow \pi^*$
		260	38,462	$\pi \rightarrow \pi^*$

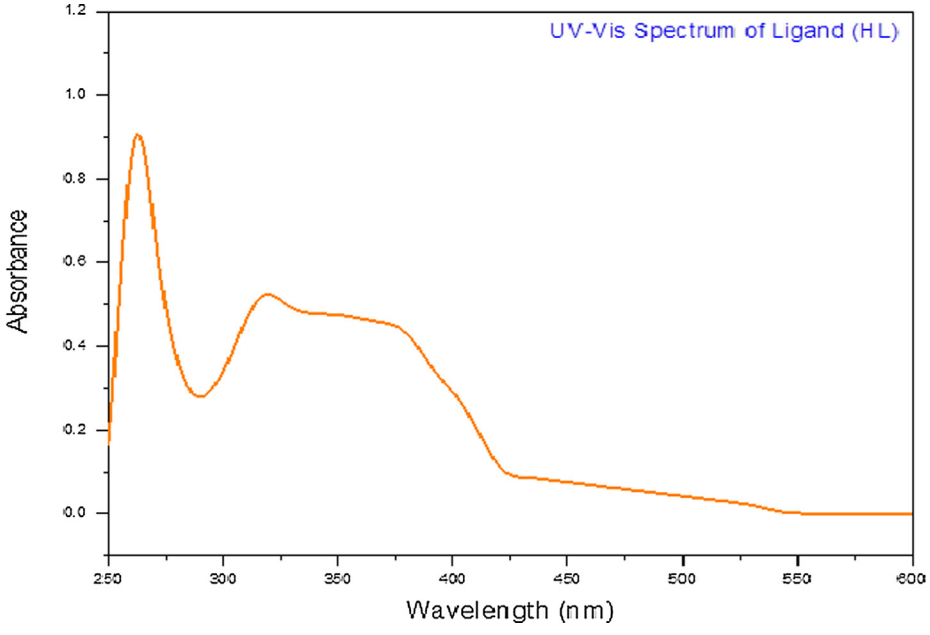

Fig. 4 UV–Vis spectrum of the ligand.

Table 4 Thermal data of the metal complexes.

Comp. No.	Temp. range (°C)	DTA (peak)		TGA (Wt. loss %)		Assignment
		Endo.	Exo.	Calc.	Found	
2	201–320	304		8.63	8.11	Loss of two chloride atoms
	321–415	393	–	42.65	42.27	Loss of one ligand (HL)
	416–466	–	428	30.48	31.63	Decomposition with the formation of V_2O_3
3	189–286	–	215	8.62	8.26	Loss of two chloride atoms
	287–416	–	299	42.60	41.93	Loss of one ligand (HL)
	417–493	747	–	30.31	31.72	Decomposition with the formation of Cr_2O_3
4	133–265	–	160	7.03	6.81	Loss of two molecules of coordination water
	266–344	–	–	13.84	14.27	Loss of two chloride atoms
	345–496	–	381	65.28	64.30	Decomposition with the formation of MnO
5	160–264	–	256	2.23	2.13	Loss of molecule of coordination water
	265–378	374	–	4.39	4.22	Loss of chloride atom
	379–498	458	–	73.62	74.20	Decomposition with the formation of Fe_2O_3
6	159–253	–	–	2.22	2.47	Loss of molecule of coordination water
	254–358	–	332	4.37	4.80	Loss of chloride atom
	459–494	468	–	72.96	72.31	Decomposition with the formation of Co_2O_3
7	179–243	–	–	2.22	2.52	Loss of molecule of coordination water
	244–361	–	341	4.37	4.88	Loss of chloride atom
	362–514	438	–	84.21	83.76	Decomposition with the formation of NiO
8	115–235	–	–	6.92	6.47	Loss of two molecules of coordination water
	236–304	–	262	13.61	14.83	Loss of two chloride atoms
	305–489	341	–	64.20	65.12	Decomposition with the formation of CuO
9	224–316	–	–	8.47	8.62	Loss of two chloride atoms
	317–465	–	382	81.82	82.13	Decomposition with the formation of ZnO

Table 5 The unit cell parameters and crystal data of the ligand and its metal complexes.

Parameters	compounds								
	HL	V(III)	Cr(III)	Mn(II)	Fe(III)	Co(III)	Ni(II)	Cu(II)	Zn(II)
a (Å)	13.179	9.878	24.02	9.692	13.62	8.148	10.082	10.66	12.550
b (Å)	11.045	9.878	8.541	10.072	13.62	9.337	20.16	12.46	12.550
c (Å)	19.731	10.20	14.44	10.300	13.62	11.259	18.92	13.93	7.13
Alfa (°)	90.0	90.0	90.0	80.57	90.0	70.13	90.0	117.8	90.0
Beta(°)	90.0	90.0	93.96	68.40	90.0	77.67	90.0	100.1	90.0
gamma(°)	90.0	120.0	90.0	76.21	90.0	86.09	90.0	94.9	120.0
Volume of unit cell($Å^3$)	2872	862	2956	904.8	2524	787	3844	1582	973
Crystal size (nm)	217	12	55	43	19	43	31	20	24
Crystal type	Orthorhombic	Hexagonal	monoclinic	Triclinic	Cubic	Triclinic	Orthorhombic	Triclinic	Hexagonal
Space group	*Pbcm*	*P*-6	*C*12 / *m*1	*P*-1	*Pa*-3	*P*-1	*P mmm*	*P*-1	*P*-6

3.2. Biology

3.2.1. In vitro anticancer activities

The in vitro cytotoxic activities of the ligand and its metal complexes towards PC-3, SKOV3 and HeLa tumour cell lines were determined using SBR assays with six different concentrations of each compound (0.01, 0.1, 1, 10, 100, and 1000 μg/mL). By comparing the results with those of a previous study (Matela, 2020), the tested compounds in the present work exhibited highly cytotoxic activity against the selected human cell lines (Fig. 10). The data in Table 6 show that the Cu(II) complex had the highest activity among the tested compounds against PC-3, SKOV3, and HeLa cells with IC_{50} values of 0.161, 0.063, and 0.087 μg/mL, respectively. Meanwhile, the Ni(II) complex exhibited the lowest toxicity towards the PC-3, SKOV3 and HeLa cells among the tested compounds, giving IC_{50} values of 1.8287, 1.2502, and 3.8453 μg/mL, respectively. On the other hand, the range of IC_{50} values of the ligand and the V(III), Cr(III), Mn(II), Fe (III), Co(III), and Zn(II) complexes for the PC-3, SKOV3, and HeLa cells were 0.1786–1.0607, 0.0615–0.8128, and 0.07 19–1.534 μg/mL, respectively. It is worth noting that the prepared compounds (**1**–**9**) exhibited higher activities than clinically used drugs such as cisplatin ($IC_{50} \sim 2.4$ μg/mL) (Ray et al., 2007), estramustine ($IC_{50} \sim 0.35$–1.3 μg/mL) (Nicholson et al., 2002), and etoposide ($IC_{50} \sim 17.4$ μg/mL) (Aras and Yerlikaya, 2016). Fig. 11 shows the cytotoxic dose–response curves for compounds **1**–**9** towards selected human cell lines where cells were exposed to the compounds at different concentrations for 72 h.

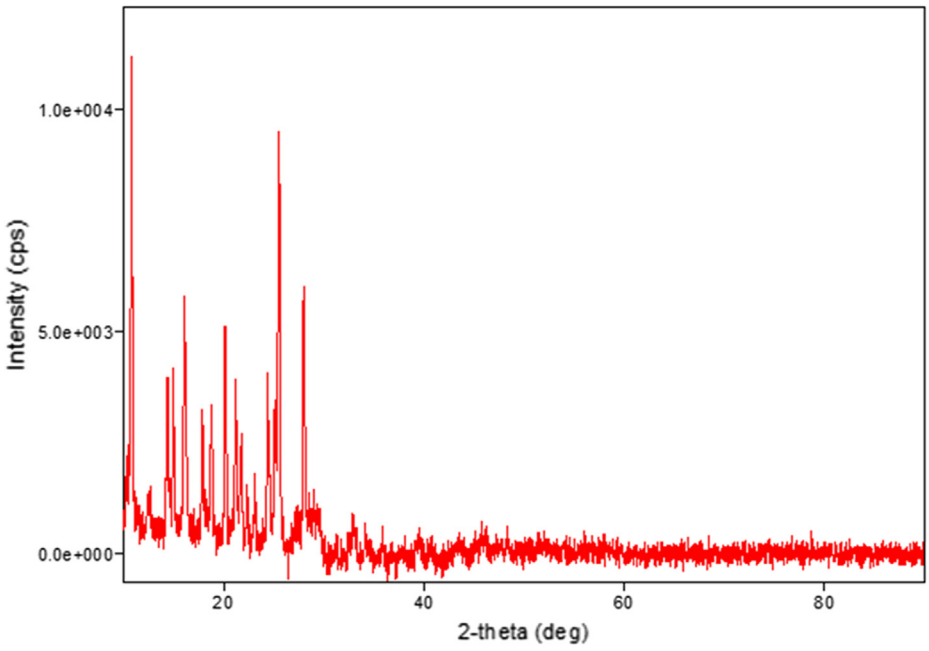

Fig. 5 XRD pattern of the Co(III) complex.

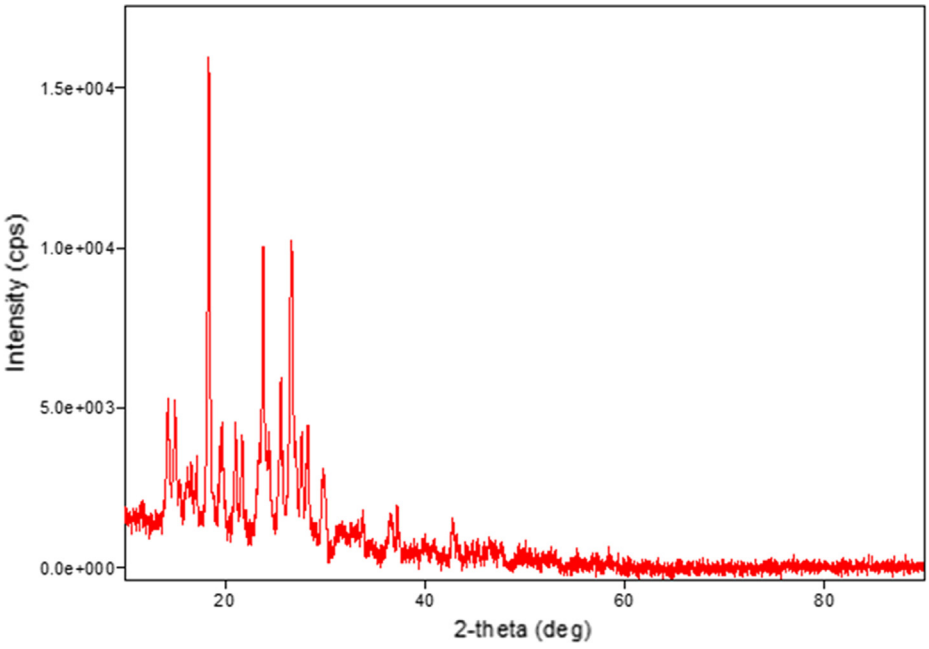

Fig. 6 XRD pattern of the Cu(II) complex.

3.2.2. Antimicrobial activity

The data in Table 7 show the antibacterial and antifungal activities of ligand and its metal complexes in different volumes against the growth of *S. enterica* ser. typhi, (Fig. 12) and *C. albicans* (Fig. 13). It was observed that the Co(III) and Zn(II) complexes had intermediate antibacterial activities against *S. enterica* ser. typhi when used in volumes of 30, 20, and 10 µL (Fig. 14). On other hand, in the same volumes, the V(III), Cr(III), Mn(II), Fe(III), Ni(II), and Cu(II) complexes and the ligand do not exhibit antibacterial activities against *S. enterica* ser. typhi. However, the V(III) complex had the highest activity against *C. albicans* when used in volumes of 30, 20, and 10 µL (Fig. 14). The Fe(III) and Cr(III) complexes also had high antifungal activities against *C. albicans* in volumes of 30 µL and 20 µL (Fig. 14). The Co(III) and Cu(II) complexes in volumes of 30, 20, and 10 µL had intermediate antifungal activities against *C. albicans*, while the Mn(II), Ni(II), and Zn(II) complexes and the ligand showed weak antifungal activities against *C. albicans* when used in the same volumes.

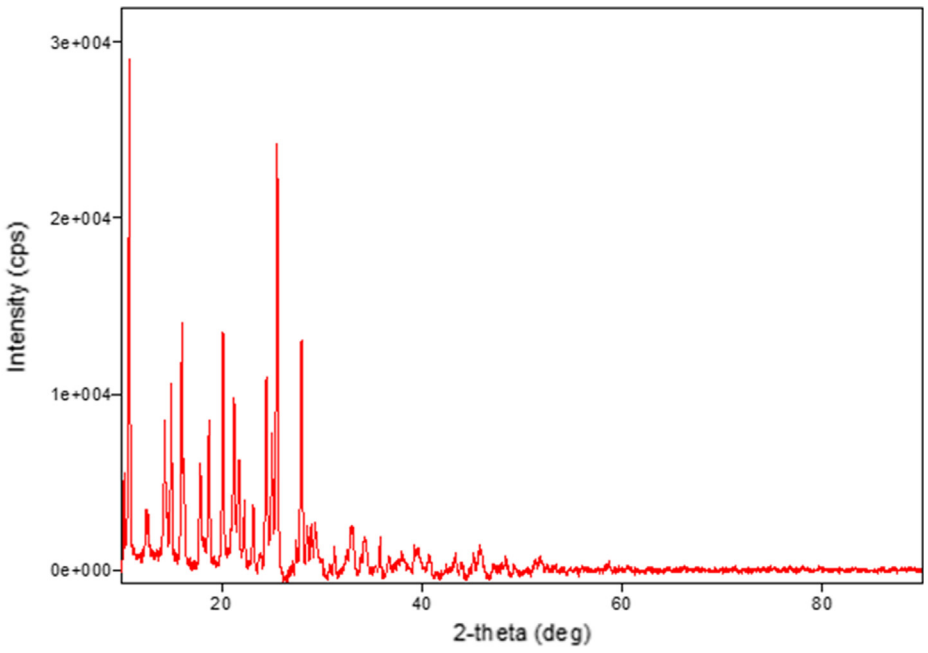

Fig. 7 XRD pattern of the Zn(II) complex.

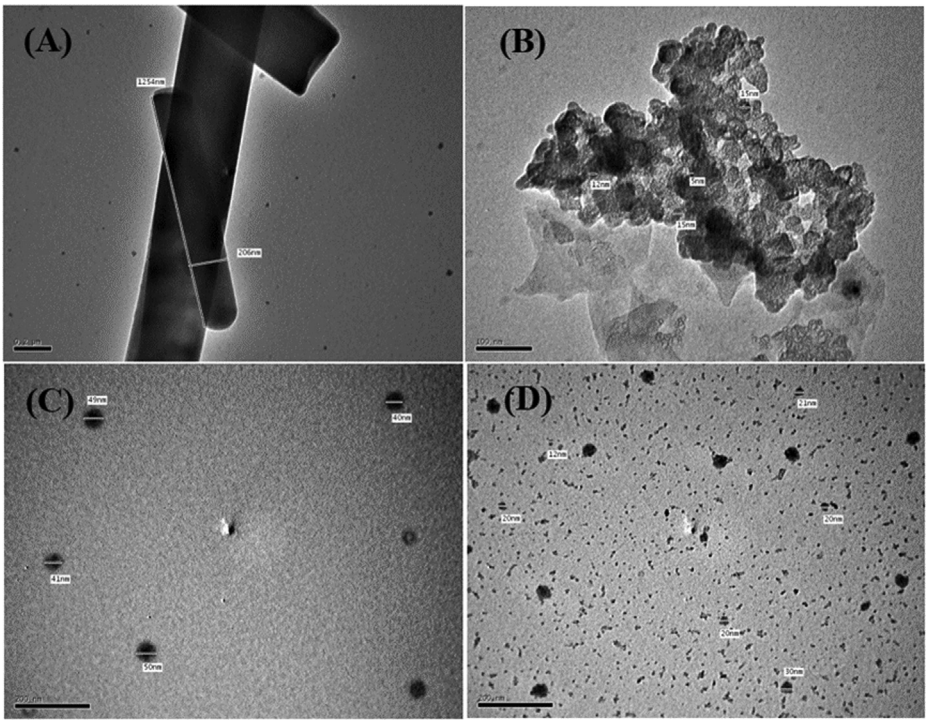

Fig. 8 High-resolution TEM images of the (A) ligand, (B)V(III) complex, (C) Mn(II) complex, and (D) Fe(III) complex.

4. Conclusion

In this work, we have synthesized a new Schiff base and employed it as a ligand in various metal complexes. Spectral, elemental, and thermal analyses, as well as conductivity measurements, confirmed that the ligand adopted bidentate behaviour and bonded with the metals through its azomethine nitrogen atom and its phenolic oxygen atom, thus exhibiting octahedral geometries. XRD analysis of the complexes indicated that they were of various structures: triclinic, orthorhombic, hexagonal, monoclinic, and cubic. TEM analysis confirmed that the metal complex powders contain both spherical and rod-shaped nanoparticles, while the ligand powder

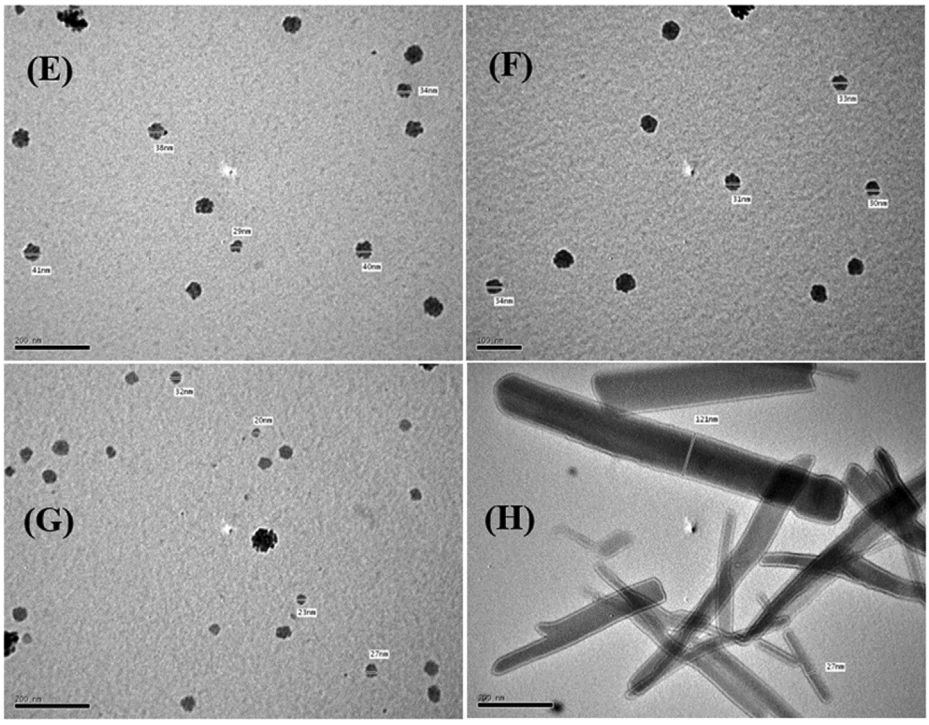

Fig. 9 High-resolution TEM images of the (E) Co(III), (F) Ni(II), (G) Cu(II), and (H) Zn(II) complexes.

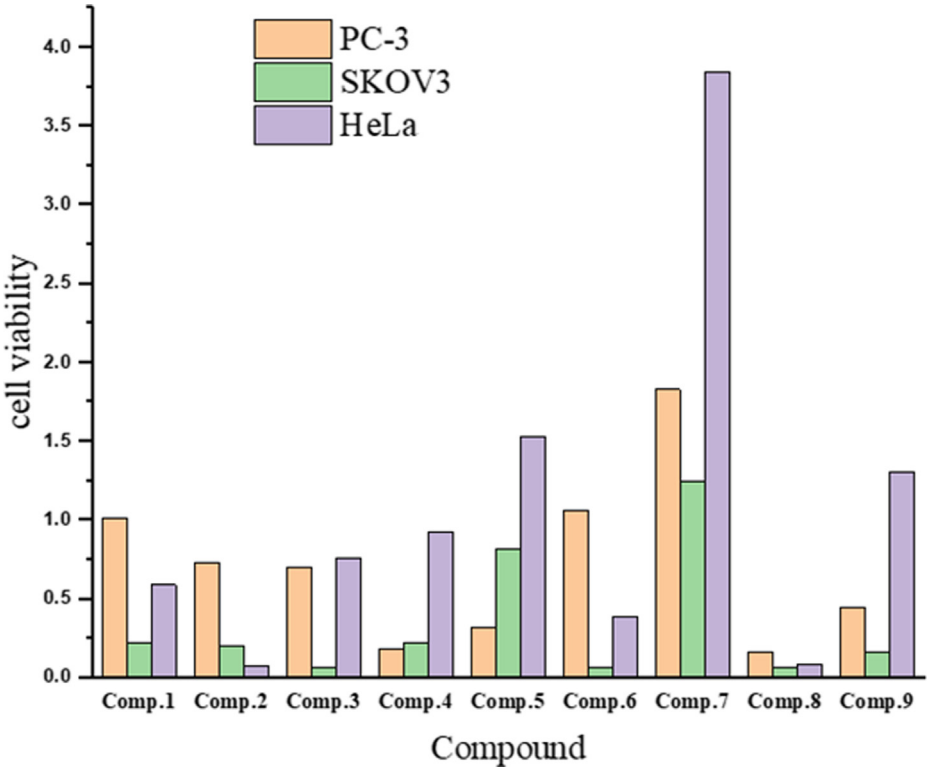

Fig. 10 Screening of anticancer activity of the ligand and its metal complexes against selected human cell lines.

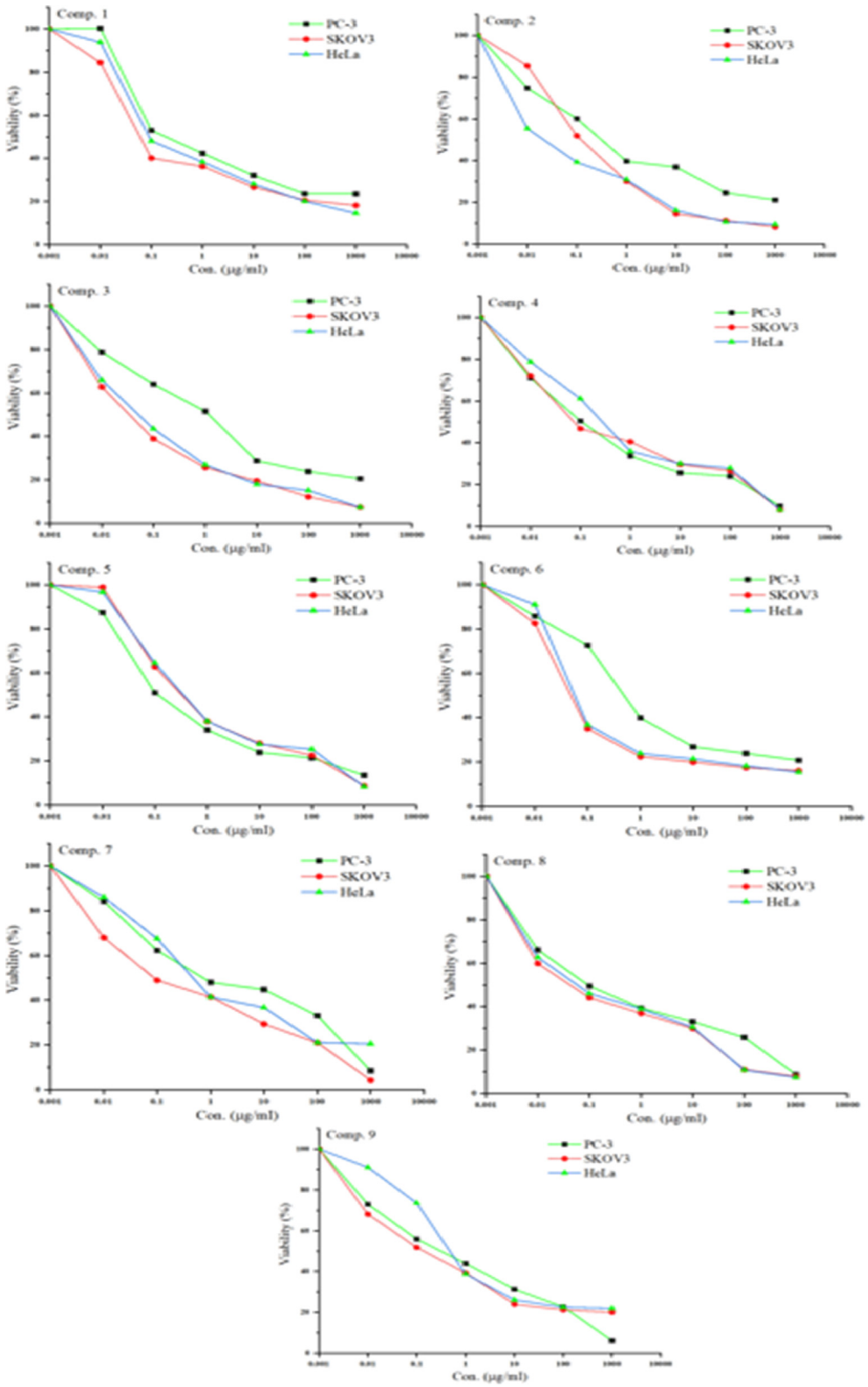

Fig. 11 The dose–response curves of the cytotoxicities of compounds **1**–**9** towards PC-3, SKOV3, and HeLa human cell lines. Cells were exposed to different concentrations of the compounds for 72 h. Cell viability was determined by sulforhodamine B (SRB) staining.

Table 6 The IC_{50} values (μg/mL) of the tested ligand and its metal complexes against different human cell lines.

No.	Compound	IC_{50} (μg/mL)		
		PC-3	SKOV3	HeLa
1	$[HL][C_{24}H_{18}N_2O]$	1.0123 ± 0.05	0.2163 ± 0.005	0.5877 ± 0.14
2	$[(HL)(L)V(Cl)_2]$	0.7262 ± 0.14	0.1997 ± 0.03	0.0719 ± 0.02
3	$[(HL)(L)Cr(Cl)_2]$	0.7027 ± 0.25	0.0678 ± 0.03	0.7606 ± 0.05
4	$[(HL)Mn(Cl)_2(H_2O)_2]$	0.1786 ± 0.02	0.2189 ± 0.05	0.9254 ± 0.05
5	$[(L)_2Fe(Cl)(H_2O)]$	0.3188 ± 0.02	0.8128 ± 0.20	1.5340 ± 0.30
6	$[(L)_2Co(Cl)(H_2O)]$	1.0607 ± 0.16	0.0615 ± 0.02	0.3921 ± 0.03
7	$[(HL)(L)Ni(Cl)(H_2O)]$	1.8287 ± 0.10	1.2502 ± 0.20	3.8453 ± 0.32
8	$[(HL)Cu(Cl)_2(H_2O)_2]$	0.1612 ± 0.005	0.0630 ± 0.003	0.0872 ± 0.01
9	$[(HL)_2Zn(Cl)_2]$	0.4436 ± 0.07	0.1646 ± 0.04	1.3064 ± 0.46

Table 7 Antibacterial and antifungal activities of different levels of the ligand and its metal complexes against the growth of *Salmonella enterica* serovar Typhi (*S. enterica* ser. Typhi) and *Candida albicans*.

No.	Compound	*Salmonella* typhi			*Candida albicans*		
		30 μL	20 μL	10 μL	30 μL	20 μL	10 μL
–	DMSO	0	0	0	0	0	0
1	$[HL][C_{24}H_{18}N_2O]$	0	0	0	4	3	2
2	$[(HL)(L)V(Cl)_2]$	0	0	0	13	12	9
3	$[(HL)(L)Cr(Cl)_2]$	0	0	0	11	10	8
4	$[(HL)Mn(Cl)_2(H_2O)_2]$	0	0	0	5	3	0
5	$[(L)_2Fe(Cl)(H_2O)]$	0	0	0	12	11	9
6	$[(L)_2Co(Cl)(H_2O)]$	9	8	7	10	9	7
7	$[(HL)(L)Ni(Cl)(H_2O)]$	0	0	0	4	3	0
8	$[(HL)Cu(Cl)_2(H_2O)_2]$	0	0	0	9	8	6
9	$[(HL)_2Zn(Cl)_2]$	7	6	5	5	4	2
–	Gentamycin	–	–	2	–	–	–
–	Clotrimazole	–	–	–	–	–	3

Note: Zone of inhibition in mm.

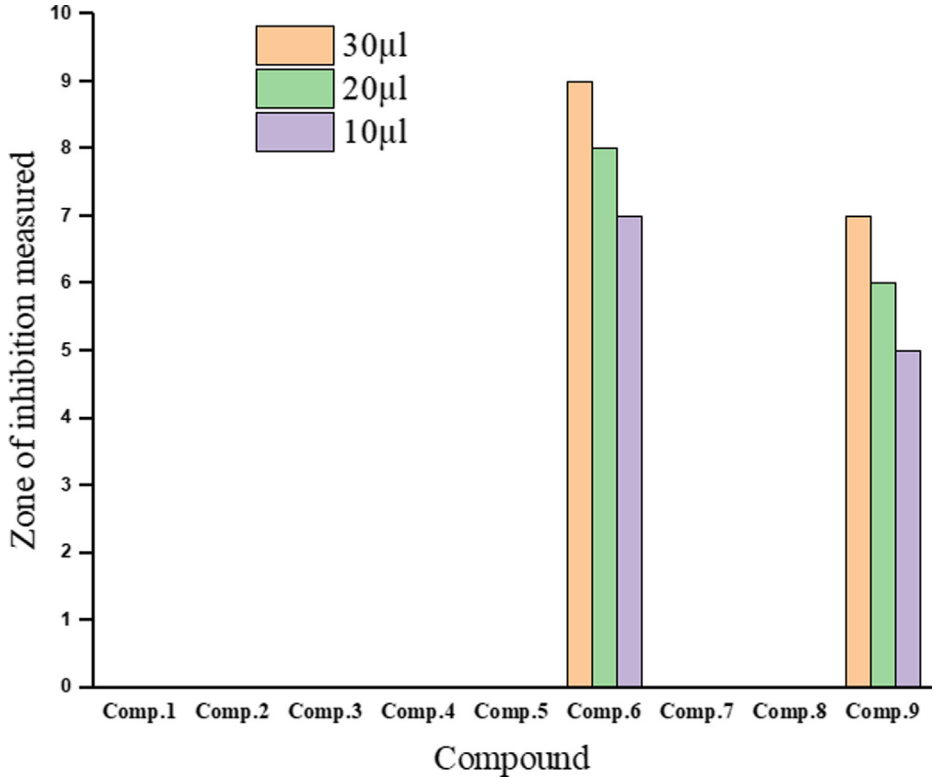

Fig. 12 Antibacterial activities of the ligand and its metal complexes.

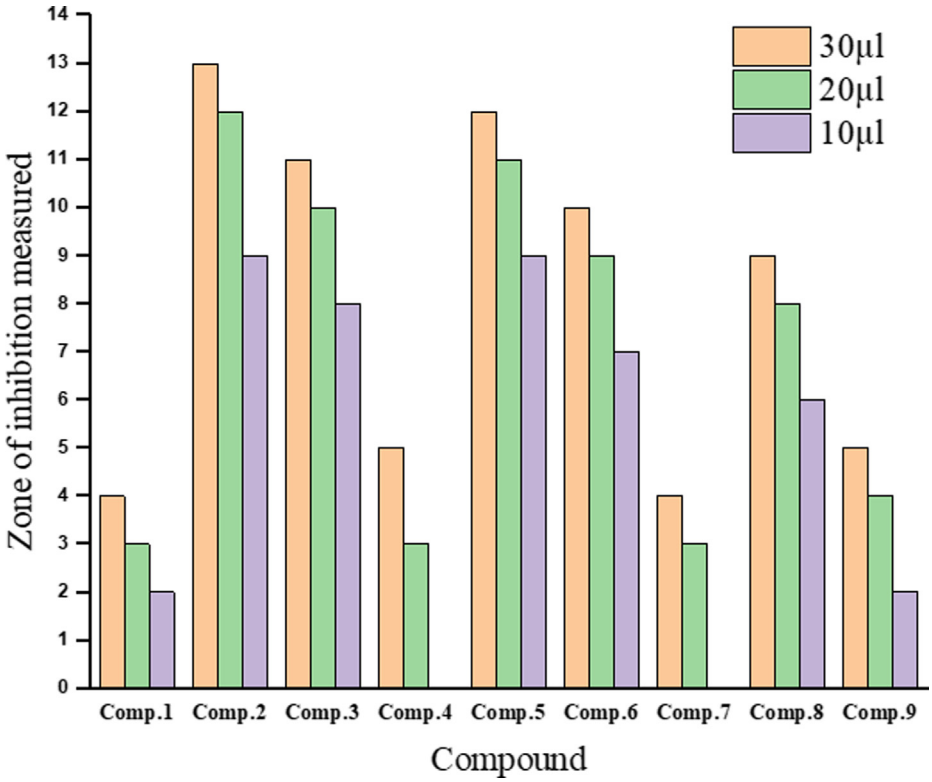

Fig. 13 Antifungal activities of the ligand and its metal complexes.

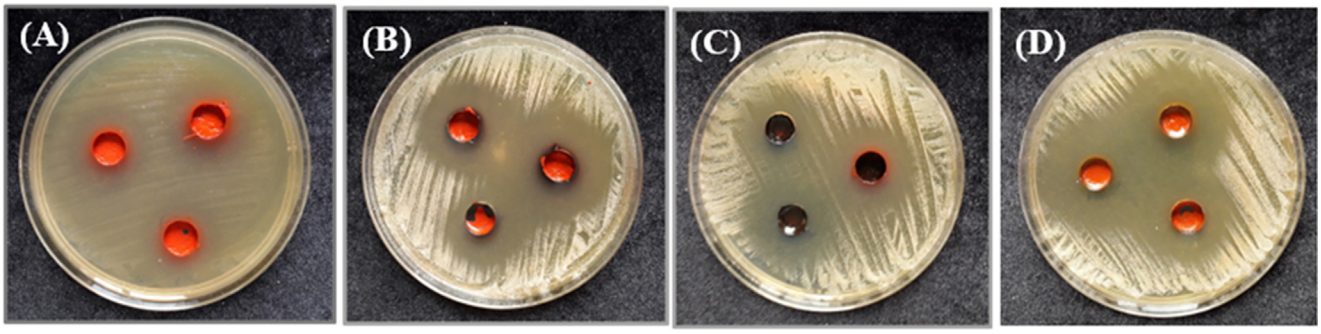

Fig. 14 Inhibition zone of the (A) Co(III) complex against *S. enterica* ser. Typhi growth, and those of the (B) V(III), (C) Fe(III), and (D) Cr(III) complexes against *C. albicans* growth.

shows rod-shaped, micro-size particles. The antibacterial and antifungal activities of the ligand and its complexes against *S. enterica* ser. typhi and *C. albicans* were investigated by the hole plate diffusion method. It was observed that the Co(III) and Zn(II) complexes had intermediate antibacterial activities, while the V(III) complex demonstrated the highest activity against *C. albicans* fungi among the tested complexes. Furthermore, the in vitro antitumor results showed that the Cu(II) complex had the highest activity among the tested compounds against PC-3, SKOV3, and HeLa cells. Remarkably, the ligand and all its metal complexes showed higher antitumour activities against these selected human cell lines than clinically used drugs such as cisplatin, estramustine, and etoposide.

Funding

This research did not receive any specific grant from funding agencies in the public, commercial, or not-for-profit sectors

References

Al-Fakeh, M.S., Amiri, N., Al-Hakemi, A.N., Saeed, S.-E.-S., Albadri, A.E.A.E., 2020. Asian J. Chem. 32, 2502–2506.

Al-Hakimi, A.N., 2020. Synthesis, characterization and microbicides activities of N(hydroxy-4-((4-nitrophenyl)diazenyl) benzylidene)-2-(phenylamino) acetohydrazide metal complexes. Egypt. J. Chem. 63, 1509–1525 https://doi.org/10.21608/ejchem.2020.20906.2256.

Al-Hakimi, A.N., Alminderej, F., Aroua, L., Alhag, S.K., Alfaifi, M. Y., M, S.O., Mahyoub, J.A., Eldin I. Elbehairi, S., Alnafisah, A.S., 2020. Design, synthesis, characterization of zirconium (IV), cadmium (II) and iron (III) complexes derived from Schiff base 2-aminomethylbenzimidazole, 2-hydroxynaphtadehyde and evaluation of their biological activity. Arab. J. Chem. 13, 7378–7389. https://doi.org/10.1016/j.arabjc.2020.08.014.

Alam, M.M., Nazreen, S., Almalki, A.S.A., Elhenawy, A.A., Alsenani, N.I., Elbehairi, S.E.I., Malebari, A.M., Alfaifi, M.Y., Alsharif, M. A., Alfaifi, S.Y.M., 2021. Naproxen based 1, 3, 4-oxadiazole derivatives as EGFR inhibitors: design, synthesis, anticancer, and computational studies. Pharmaceuticals 14, 870.

Alhakimi, A.N., Shakdofa, M.M.E., Saeed, S., Shakdofa, A.M.E., Al-Fakeh, M.S., Abdu, A.M., Alhagri, I.A., 2021. Transition metal complexes derived from 2-hydroxy-4-(p-tolyldiazenyl) benzylidene)-2-(p-tolylamino) acetohydrazide synthesis, structural characterization, and biological activities. J. Korean Chem. Soc. 65, 93–105.

Aly, A.A.M., Ghandour, M.A., Al-Fakeh, M.S., 2012. Synthesis and characterization of transition metal coordination polymers derived from 1,4-benzenedicarboxylate and certain azoles. Turkish J. Chem. 36, 69–79. https://doi.org/10.3906/kim-1106-61.

Aras, B., Yerlikaya, A., 2016. Bortezomib and etoposide combinations exert synergistic effects on the human prostate cancer cell line PC-3. Oncol. Lett. 11, 3179–3184.

Azam, M., Al-resayes, S.I., Trzesowska-Kruszynska, A., Kruszynski, R., Shakeel, F., Soliman, S.M., Alam, M., Khan, M.R., Wabaidur, S.M., 2020. Zn (II) complex derived from bidentate Schiff base ligand: synthesis, characterization, DFT studies and evaluation of anti-in flammatory activity. J. Mol. Struct. 1201, 127177. https://doi.org/10.1016/j.molstruc.2019.127177.

Betiha, M.A., El-Henawy, S.B., Al-Sabagh, A.M., Negm, N.A., Mahmoud, T., 2020. Experimental evaluation of cationic-Schiff base surfactants based on 5-chloromethyl salicylaldehyde for improving crude oil recovery and bactericide. J. Mol. Liq. 316, 113862. https://doi.org/10.1016/j.molliq.2020.113862.

Bhaskar, R.S., Ladole, C.A., Salunkhe, N.G., Barabde, J.M., Aswar, A.S., 2020. Synthesis, characterization and antimicrobial studies of novel ONO donor hydrazone Schiff base complexes with some divalent metal (II) ions. Arab. J. Chem. 13, 6559–6567. https://doi.org/10.1016/j.arabjc.2020.06.012.

Bocian, A., Skrodzki, M., Kubicki, M., Gorczyński, A., Pawluć, P., Patroniak, V., 2020. The effect of Schiff base ligands on the structure and catalytic activity of cobalt complexes in hydrosilylation of olefins. Appl. Catal. A Gen. 602, 117665. https://doi.org/10.1016/j.apcata.2020.117665.

Buldurun, K., Turan, N., Bursal, E., Mantarcı, A., Turkan, F., Taslimi, P., Gülçin, İ., 2020. Synthesis, spectroscopic properties, crystal structures, antioxidant activities and enzyme inhibition determination of Co(II) and Fe(II) complexes of Schiff base. Res. Chem. Intermed. 46, 283–297. https://doi.org/10.1007/s11164-019-03949-3.

Chauhan, D.S., Mazumder, M.A.J., Quraishi, M.A., Ansari, K.R., 2020. Chitosan-cinnamaldehyde Schiff base: a bioinspired macromolecule as corrosion inhibitor for oil and gas industry. Int. J. Biol. Macromol. 158, 127–138. https://doi.org/10.1016/j.ijbiomac.2020.04.200.

Dorn, M., Kalmbach, J., Boden, P., Päpcke, A., Gómez, S., Förster, C., Kuczelinis, F., Carrella, L.M., Büldt, L.A., Bings, N.H., Rentschler, E., Lochbrunner, S., González, L., Gerhards, M., Seitz, M., Heinze, K., 2020. A vanadium(III) complex with blue and NIR-II spin-flip luminescence in solution. J. Am. Chem. Soc. 142, 7947–7955. https://doi.org/10.1021/jacs.0c02122.

El-Saied, F.A., Salem, T.A., Shakdofa, M.M.E., Al-Hakimi, A.N., Radwan, A.S., 2018a. Antitumor activity of synthesized and characterized Cu (II), Ni (II) and Co (II) complexes of hydrazone-oxime ligands derived from 3-(hydroxyimino) butan-2-one. Beni-Suef Univ. J. basic Appl. Sci. 7, 420–429.

El-Shafiy, H.F., Saif, M., Mashaly, M.M., Halim, S.A., Eid, M.F., Nabeel, A.I., Fouad, R., 2017. New nano-complexes of Zn (II), Cu (II), Ni (II) and Co (II) ions; spectroscopy, thermal, structural analysis, DFT calculations and antimicrobial activity application. J. Mol. Struct. 1147, 452–461.

El-Tabl, A.S., 2002. Synthesis, characterisation and antimicrobial activity of manganese (II), nickel (II), cobalt (II), copper (II) and zinc (II) complexes of a binucleating tetradentate ligand. J. Chem. Res. 2002, 529–531.

El-Tabl, A.S., El-Saied, F.A., Al-Hakimi, A.N., 2008. Spectroscopic characterization and biological activity of metal complexes with an ONO trifunctionalized hydrazone ligand. J. Coord. Chem. 61, 2380–2401.

El-tabl, A.S., El-saied, F.A., Plass, W., Al-hakimi, A.N., 2008. Synthesis, spectroscopic characterization and biological activity of the metal complexes of the Schiff base derived from phenylaminoacetohydrazide and dibenzoylmethane. Spectrochim Acta Part A Mol. Biomol. Spectrosc. 71, 90–99. https://doi.org/10.1016/j.saa.2007.11.011.

El-Saied, F.A., Salem, T.A., Shakdofa, M.M.E., Al-Hakimi, A.N., 2018b. Anti-neurotoxic evaluation of synthetic and characterized metal complexes of thiosemicarbazone derivatives. Appl. Organomet. Chem. 32, e4215.

El-saied, F.A., Shakdofa, M.M.E., Al-Hakimi, A.N., Shakdofa, A.M. E., 2020. Transition metal complexes derived from N′-(4-fluorobenzylidene)-2-(quinolin-2-yloxy) acetohydrazide: Synthesis, structural characterization, and biocidal evaluation. Appl. Organomet. Chem. 34, e5898.

El Malti, J., Mountassif, D., Amarouch, H., 2007. Antimicrobial activity of Elettaria cardamomum: toxicity, biochemical and histological studies. Food Chem. 104, 1560–1568.

Gachkar, L., Yadegari, D., Rezaei, M.B., Taghizadeh, M., Astaneh, S. A., Rasooli, I., 2007. Chemical and biological characteristics of Cuminum cyminum and Rosmarinus officinalis essential oils. Food Chem. 102, 898–904.

Ghfar, A.A., El-Metwally, M.M., Shaaban, M., Gabr, S.A., Gabr, N. S., Diab, M.S.M., Aqel, A., Habila, M.A., Al-Qahtani, W.H., Alfaifi, M.Y., 2021. Production of terretonin N and butyrolactone I by thermophilic aspergillus terreus TM8 promoted apoptosis and cell death in human prostate and ovarian cancer cells. Molecules 26, 2816.

Güngör, Ö., Gürkan, P., 2019. Potentiometric and antimicrobial studies on the asymmetric Schiff bases and their binuclear Ni(II) and Fe(III) complexes; synthesis and characterization of the complexes. Arab. J. Chem. 12, 2244–2256. https://doi.org/10.1016/j.arabjc.2015.02.009.

Hanbali, F.E.L., Akssira, M., Ezoubeiri, A., Mellouki, F., Benherraf, A., Blazquez, A.M., Boira, H., 2005. Chemical composition and antibacterial activity of essential oil of Pulicaria odora L. J. Ethnopharmacol. 99, 399–401.

Hosseinzadeh Sanatkar, T., Khorshidi, A., Sohouli, E., Janczak, J., 2020. Synthesis, crystal structure, and characterization of two Cu (II) and Ni(II) complexes of a tetradentate N2O2 Schiff base ligand and their application in fabrication of a hydrazine electrochemical sensor. Inorganica Chim. Acta 506, 119537. https://doi.org/10.1016/j.ica.2020.119537.

Kavitha, P., Laxma Reddy, K., 2016. Pd(II) complexes bearing chromone based Schiff bases: synthesis, characterisation and biological activity studies. Arab. J. Chem. 9, 640–648. https://doi.org/10.1016/j.arabjc.2013.06.018.

Keypour, H., Mahmoudabadi, M., Shooshtari, A., Bayat, M., Soltani, E., Karamian, R., Farida, S.H.M., 2020. Synthesis, spectral, theoretical and antioxidant studies of copper (II) and cobalt (III) macroacyclic Schiff-base complexes containing homopiperazine moietiy. Chem. Data Collect. 26, 100354. https://doi.org/10.1016/j.cdc.2020.100354.

Kobisy, A.S., Nassar, H.N., Tawfik, S.M., Elshatoury, E.H., Aiad, I., 2020. Mitigation of eco-unfriendly and costly microbial induced

corrosion using novel synthesized Schiff base cationic surfactants. J. Chem. Technol. Biotechnol.

Magwa, M.L., Gundidza, M., Gweru, N., Humphrey, G., 2006. Chemical composition and biological activities of essential oil from the leaves of Sesuvium portulacastrum. J. Ethnopharmacol. 103, 85–89. https://doi.org/10.1016/j.jep.2005.07.024.

Mahmoud, W.H., Omar, M.M., Ahmed, Y.M., Mohamed, G.G., 2020. Transition metal complexes of Schiff base ligand based on 4, 6-diacetyl resorcinol. Appl. Organomet. Chem. 34, e5528.

Malik, M.A., Lone, S.A., Gull, P., Dar, O.A., Wani, M.Y., Ahmad, A., Hashmi, A.A., 2018. Efficacy of novel Schiff base derivatives as antifungal compounds in combination with approved drugs against candida albicans. Med. Chem. (Los. Angeles). 15, 648–658. https://doi.org/10.2174/1573406415666181203115957.

Manimohan, M., Pugalmani, S., Aboobucker, M., Sithique, M.A., 2020. Biologically active water soluble novel biopolymer/hydrazide based O -carboxymethyl chitosan schiff bases: synthesis and characterisation. J. Inorg. Organomet. Polym. Mater. 30, 3658–3676. https://doi.org/10.1007/s10904-020-01487-9.

Matela, G., 2020. Schiff bases and complexes: a review on anti-cancer activity. Anti-Cancer Agents Med Chem. (Formerly Curr. Med. Chem. Agents) 20, 1908–1917.

Maurya, R.C., Chourasia, J., Rajak, D., Malik, B.A., Mir, J.M., Jain, N., Batalia, S., 2016. Oxovanadium(IV) complexes of bioinorganic and medicinal relevance: synthesis, characterization and 3D molecular modeling of some oxovanadium(IV) complexes involving O, N-donor environment of salicylaldehyde-based sulfa drug Schiff bases. Arab. J. Chem. 9, S1084–S1100. https://doi.org/10.1016/j.arabjc.2011.12.012.

Mbugua, S.N., Sibuyi, N.R.S., Njenga, L.W., Odhiambo, R.A., Wandiga, S.O., Meyer, M., Lalancette, R.A., Onani, M.O., 2020. New palladium(II) and platinum(II) complexes based on pyrrole Schiff bases: synthesis, characterization, X-ray structure, and anticancer activity. ACS Omega 5, 14942–14954. https://doi.org/10.1021/acsomega.0c00360.

Mondal, B., Banerjee, S., Ray, J., Jana, S., Senapati, S., Tripathy, T., 2020. Novel dextrin-cysteine Schiff base: a highly efficient sensor for mercury ions in aqueous environment. ChemistrySelect 5, 2082–2093.

Mosa'd Jamil, Y., Al-Maqtari, M.A., Al-Azab, F.M., Al-Qadasy, M. K., Al-Gaadbi, A.A., 2018. Synthesis, Characterization and comparative thermal degradation study of Co (II), Ni (II) and Cu (II) complexes with Asparagine and Urea as mixed ligands. Eclética Química J. 43, 11–24.

Murukan, B., Mohanan, K., 2006. Synthesis, characterization, electrochemical properties and antibacterial activity of some transiton metal complexes with [(2-hydroxy-1-naphthaldehyde)-3-isatin]-bishydrazone. Transit. Met. Chem. 31, 441–446.

Nagalakshmi, V., Sathya, M., Premkumar, M., Kaleeswaran, D., Venkatachalam, G., Balasubramani, K., 2020. Palladium(II) complexes comprising naphthylamine and biphenylamine based Schiff base ligands: synthesis, structure and catalytic activity in Suzuki coupling reactions. J. Organomet. Chem. 914, 121220. https://doi.org/10.1016/j.jorganchem.2020.121220.

Nicholson, K.M., Phillips, R.M., Shnyder, S.D., Bibby, M.C., 2002. In vitro and in vivo activity of LS 4477 and LS 4559, novel analogues of the tubulin binder estramustine. Eur. J. Cancer 38, 194–204. https://doi.org/10.1016/S0959-8049(01)00341-0.

Radha, V.P., Chitra, S., Jonekirubavathi, S., Chung, I.-M., Kim, S.-H., Prabakaran, M., 2020. Transition metal complexes of novel binuclear Schiff base derived from 3,3′-diaminobenzidine: synthesis, characterization, thermal behavior, DFT, antimicrobial and molecular docking studies. J. Coord. Chem. 73, 1009–1027. https://doi.org/10.1080/00958972.2020.1752372.

Ray, S., Mohan, R., Singh, J.K., Samantaray, M.K., Shaikh, M.M., Panda, D., Ghosh, P., 2007. Anticancer and antimicrobial metallopharmaceutical agents based on palladium, gold, and silver N-heterocyclic carbene complexes. J. Am. Chem. Soc. 129, 15042–15053. https://doi.org/10.1021/ja075889z.

Ren, S., Zhang, S., Zhao, W., Wang, W., 2020. High-performance naphthalenediamine-based polybenzoxazine and its cured epoxy resin. J. Mater. Sci. 55, 806–816.

Saeed, S.E., Abdel-Mottaleb, M.M.S., Abdel-Mottaleb, M.S.A., 2014. One-step thermolysis synthesis of divalent transition metal ions monodoped and tridoped CdS and ZnS luminescent nanomaterials. J. Nanomater. 2014.

Shakdofa, M.M.E., El-Saied, F.A., Rasras, A.J., Al-Hakimi, A.N., 2018. Transition metal complexes of a hydrazone–oxime ligand containing the isonicotinoyl moiety: synthesis, characterization and microbicide activities. Appl. Organomet. Chem. 32, e4376.

Shakdofa, M.M.E., Morsy, N.A., Rasras, A.J., Al-Hakimi, A.N., Shakdofa, A.M.E., 2021. Synthesis, characterization, and density functional theory studies of hydrazone–oxime ligand derived from 2, 4, 6-trichlorophenyl hydrazine and its metal complexes searching for new antimicrobial drugs. Appl. Organomet. Chem. 35, e6111.

Singh, K., Kumar, Y., Puri, P., Sharma, C., Aneja, K.R., 2017. Antimicrobial, spectral and thermal studies of divalent cobalt, nickel, copper and zinc complexes with triazole Schiff bases. Arab. J. Chem. 10, S978–S987. https://doi.org/10.1016/j.arabjc.2012.12.038.

Slassi, S., El-Ghayoury, A., Aarjane, M., Yamni, K., Amine, A., 2020. New copper (II) and zinc (II) complexes based on azo Schiff base ligand: Synthesis, crystal structure, photoisomerization study and antibacterial activity. Appl. Organomet. Chem. 34, e5503.

Tarafder, M.T.H., Ali, M.A., Wee, D.J., Azahari, K., Silong, S., Crouse, K.A., 2000. Complexes of a tridentate ONS Schiff base. Synthesis and biological properties. Transit. Met. Chem. 25, 456–460. https://doi.org/10.1023/A:1007062409973.

Yang, Z.-Y., Yang, R.-D., Li, F.-S., Yu, K.-B., 2000. Crystal structure and antitumor activity of some rare earth metal complexes with Schiff base. Polyhedron 19, 2599–2604. https://doi.org/10.1016/S0277-5387(00)00562-3.

Zaman Brohi, R.O., Khuhawar, M.Y., Mahar, R.B., 2020. Graphene oxide functionalized with a Schiff Base for the removal of Pb (II) ions from contaminated water: experimental and modeling approach. J. Chem. Technol. Biotechnol. 95, 1694–1704.